

# Disparity Estimation Using a Quad-Pixel Sensor

Zhuofeng Wu<sup>1</sup>

zww@ok.sc.e.titech.ac.jp

Doehyung Lee<sup>1</sup>

dlee@ok.sc.e.titech.ac.jp

Zihua Liu<sup>1</sup>

zliu@ok.sc.e.titech.ac.jp

Kazunori Yoshizaki<sup>2</sup>

kazunori.yoshizaki@olympus.com

Yusuke Monno<sup>1</sup>

ymonno@ok.sc.e.titech.ac.jp

Masatoshi Okutomi<sup>1</sup>

moxo@ctrl.titech.ac.jp

<sup>1</sup> Institute of Science Tokyo

Tokyo, Japan

<sup>2</sup> Olympus Medical Systems Corporation

Tokyo, Japan

## Abstract

A quad-pixel (QP) sensor is increasingly integrated into commercial mobile cameras. The QP sensor has a unit of  $2 \times 2$  four photodiodes under a single microlens, generating multi-directional phase shifting when out-focus blurs occur. Similar to a dual-pixel (DP) sensor, the phase shifting can be regarded as stereo disparity and utilized for depth estimation. Based on this, we propose a QP disparity estimation network (QPDNet), which exploits abundant QP information by fusing vertical and horizontal stereo-matching correlations for effective disparity estimation. We also present a synthetic pipeline to generate a training dataset from an existing RGB-Depth dataset. Experimental results demonstrate that our QPDNet outperforms state-of-the-art stereo and DP methods. Our code and synthetic dataset are available at <https://github.com/Zhuofeng-Wu/QPDNet>.

## 1 Introduction

Recent advancements in sensor technology have led to the gradual integration of dual-pixel (DP) [8] and quad-pixel (QP) [19] sensors into commercial digital cameras and smartphones. As shown in Fig. 1, a QP sensor has a unit of  $2 \times 2$  photodiodes under a single microlens and an identical color filter. Akin to a DP sensor, where  $1 \times 2$  photodiodes are used, the QP sensor generates phase shifting when out-focus blurs occur. The phase-shifting information is validated to be valuable in DP sensors and various applications, such as defocus deblurring [1], reflection removal [2], and raindrop removal [3], have been proposed.

Another high-potential application is depth estimation because the out-focus phase shifting can be regarded as stereo disparity. While the DP sensor only utilizes horizontal disparity

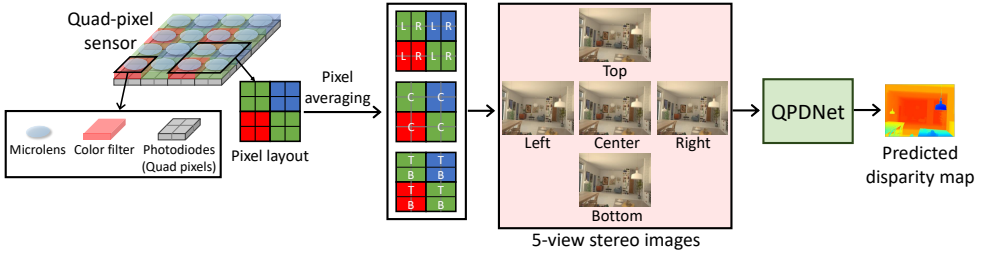


Figure 1: The overall flow of our disparity estimation. From the data captured by a QP sensor, we generate five-view stereo images, where disparities exist between a reference center image and each of the left, the right, the top, and the bottom images, according to the phase shifting principle of the DP/QP sensor in out-focus regions [19]. Using those five-view images as inputs, our QPDNet predicts a disparity map aligned to the reference center image.

in depth estimation [8, 9, 23, 28], the QP sensor can exploit multi-directional disparities using the  $2 \times 2$  photodiodes structure. Consequently, the QP sensor provides a functionality similar to a multi-baseline stereo [20] and a camera array [2] only using a single sensor. Despite this potential, as far as we know, no literature has been published yet for disparity estimation using a QP sensor.

In this paper, we propose a QP disparity estimation network (QPDNet), which effectively utilizes multi-directional disparities observed using a QP sensor. As shown in Fig. 1, we first apply three kinds of pixel averaging of raw pixel values and generate five-view (i.e., left, right, center, top, and bottom) stereo images, where the center image is used as a reference to integrate two horizontal (center-right and center-left) and two vertical (center-top and center-bottom) disparity information. Inspired by the success of RAFT-Stereo [13], we propose to construct four-directional correlation pyramids and effectively fuse them by introducing a novel multi-direction lookup fusion (MDLF) module, which is designed to extract local correlations in multiple directions and to enable adaptive fusion of extracted correlations by utilizing both channel-wise and pixel-wise attention mechanisms. As in RAFT-Stereo, the local correlations output by the MDLF module along with the current disparity and context features are iteratively fed to gated recurrent units (GRUs) to predict a final disparity map.

While some studies constructed datasets for depth estimation with DP sensors [8, 9, 23, 28], they cannot be directly used for QP sensors, because only left and right image pairs are provided. Thus, we rebuild a synthetic pipeline to generate a QP image along with a ground-truth disparity map using the pair of an all-in-focus image and a ground-truth depth map available in existing RGB-D datasets [25], by following the DP blur kernel and image formation modeling of [9]. The generated datasets are used for the training and the evaluation of our QPDNet.

In summary, our main contributions are listed as follows:

- We proposed QPDNet, a novel network to effectively predict a disparity map from QP data by combining horizontal and vertical disparities observed by a QP sensor.
- We proposed MDLF module, a novel module to effectively extract and fuse the multi-directional stereo-matching correlations.
- We constructed a dataset for disparity estimation from QP data based on a forward image formation process for the QP sensor.
- We experimentally validated that QPDNet outperforms other state-of-the-art stereo and DP methods in both synthetic and real experiments.

## 2 Related Work

### 2.1 Stereo Disparity Estimation

Given a pair of rectified stereo images, stereo matching aims to compute the disparity for each pixel in the reference image. Recently, CNN-based stereo methods [6, 12, 15, 31, 33] have achieved impressive performance on most of the standard benchmarks. Most of them construct a cost volume in the feature level to measure the matching similarity. The pioneering work DispNetC [17] utilizes a correlation layer to calculate the inner product of left and right features at each disparity level for measuring the similarity. GCNet [18] pioneered the use of concatenated left and right image features to construct a 4D volume, enriching content representation for similarity assessment. This approach, featuring a concatenation volume followed by stacked 3D convolutional networks for aggregation, has been widely adopted in many contemporary state-of-the-art methods, such as [9, 26, 33]. Building on this, GwcNet [8] and ACVNet [30] integrate the strengths of both correlation and concatenation volumes using a group-wise correlation strategy. Recent advancements [12, 15, 31] have incorporated attention mechanisms within Transformers, employing cross-attention [9] to replace traditional cost volumes. Although deep-learning-based stereo matching has achieved significant progress, the inherent nature of stereo images, which provide information from only two limited views and one matching direction, often leads to unsatisfactory results, as evidenced by that a multi-baseline stereo [20] improves the robustness.

### 2.2 DP Disparity Estimation

As DP sensors have become adopted in consumer cameras and smartphones, an increasing number of studies have emerged aiming to estimate depth/disparity from a DP image. As an early study, Wadhwa et al. adapted classical stereo-matching techniques to infer a disparity map from two DP views [28]. Punnappurath et al. modeled the defocus-disparity characteristic of the DP sensor and introduced a model-based optimization method to estimate the defocus map, which can be interpreted as an inverse depth map [23]. Xin et al. proposed another technique for estimating a defocus map by optimizing a multiplane image representation to best explain the observed DP image using the calibrated point spread function (PSF) kernels [29]. In recent years, learning-based methods have demonstrated superior performance. Garg et al. devised a learning-based approach for DP depth estimation, employing an affine invariant objective function to estimate inverse depth [5]. Pan et al. introduced an end-to-end network capable of jointly estimating depth and producing a de-blurred image [21]. Kang et al. proposed a network to estimate the depth and surface normal focusing on faces [8]. Kim et al. proposed a self-supervised learning method leveraging the symmetric property of DP PSF kernels [9].

The closest work to ours is the one by Zhang et al. [34], which applies two vertically aligned cameras, where one of the cameras is a DP camera. This configuration provides vertical disparities as a standard stereo and horizontal disparities as a DP stereo. While this configuration can leverage the different baseline lengths of the standard stereo and the DP stereo, it requires the alignment between the stereo and the DP setups due to the necessity of stereo rectification for two cameras. In contrast, our configuration using a single QP camera eliminates the need for the rectification and the alignment to handle the vertical and the horizontal disparities by using the center image as a reference image, thus making the overall system and method simpler.

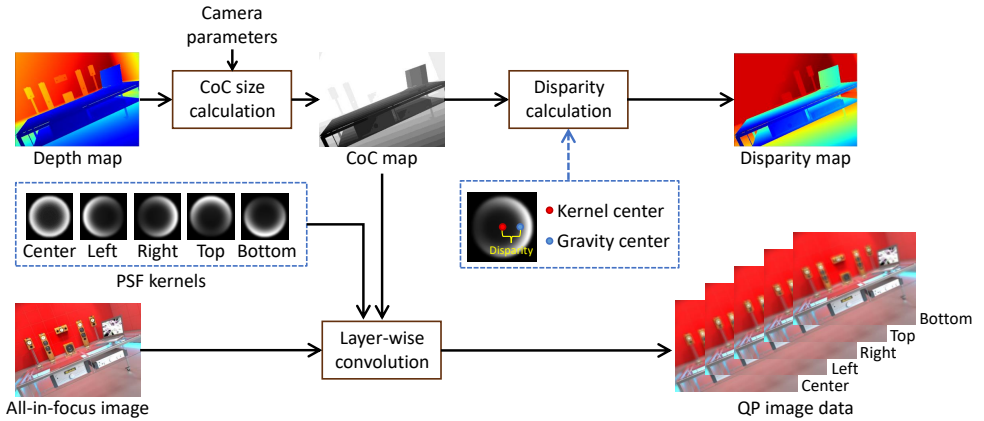


Figure 2: The overview of our data generation process.

### 3 QP Disparity Estimation Dataset Generation

Since a dataset specifically tailored for QP disparity estimation is currently unavailable, we design a synthetic data generation pipeline, as depicted in Fig. 2. The inputs are the pair of a depth map and an all-in-focus image, which is widely available in existing RGB-D datasets [25, 27, 65]. Using the depth map and the considered camera parameters, the circle-of-confusion (CoC) radius of each pixel is calculated as

$$CoC = \frac{1}{p} \times \frac{f}{2F} \times \frac{f}{f_d - f} \times \frac{z - f_d}{z}, \quad (1)$$

where  $z$  represents the depth.  $f$ ,  $f_d$ ,  $F$ , and  $p$  denote the camera's focal length, focal distance, F-stop (aperture), and pixel size, respectively.

Subsequently, we adopt DP left and right PSF kernel models of [10] and rotate them by  $90^\circ$  to generate the PSFs for the top and the bottom images. The PSF for the center image is also generated by averaging the left and the right kernels. Then, the corresponding all-in-focus image is convolved with the PSFs of each image in a layer-wise manner of [11, 12] to generate a set of five images. Finally, we define the disparity as the distance between the kernel center and the gravity center of the right PSF and compute the disparity of each pixel with the corresponding CoC size.

## 4 Proposed QPDNet

## 4.1 Network Architecture Overview

Figure 3 presents the overall architecture of our QPDNet. We employ RAFT-Stereo [14] as our baseline architecture. We use the center image as the reference image and apply two feature encoders to extract the features  $\{\mathbf{F}_l, \mathbf{F}_{c_b}, \mathbf{F}_r\}$  for horizontal matching between center-left and center-right image pairs and the features  $\{\mathbf{F}_t, \mathbf{F}_{c_v}, \mathbf{F}_b\}$  for vertical matching between center-top and center-bottom image pairs, respectively. The dimension of each feature is  $H \times W \times N_F$ , where  $H$  and  $W$  represent the image height and width, respectively, and  $N_F$  is the number of channels (specifically,  $N_F = 256$ ). Subsequently, we calculate four correlation

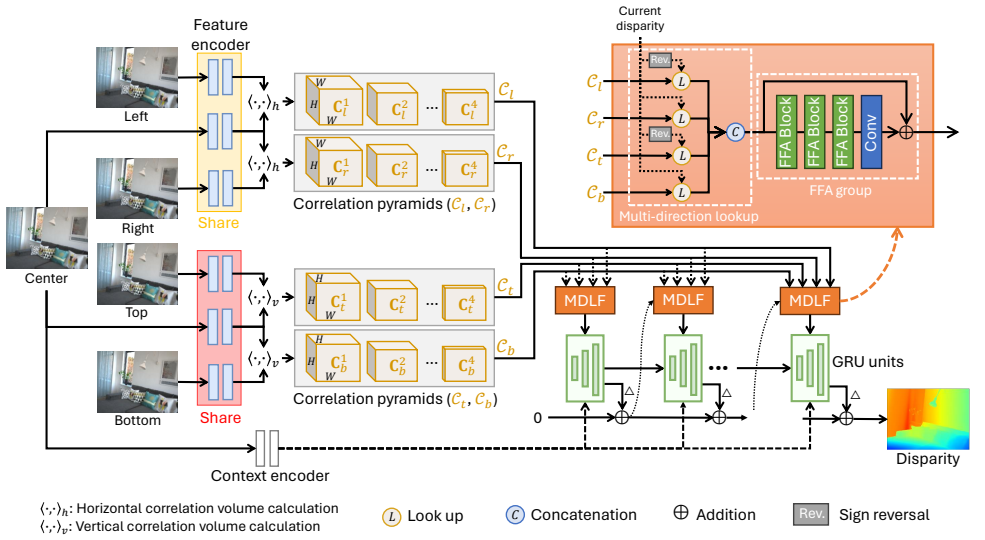


Figure 3: The overall architecture of our QPDNet.

volumes  $\{C_l, C_r, C_t, C_b\}$  as

$$C_i = \begin{cases} \langle \mathbf{F}_{c_h}, \mathbf{F}_i \rangle_h & \text{if } i \in \{l, r\}, \\ \langle \mathbf{F}_{c_v}, \mathbf{F}_i \rangle_v & \text{if } i \in \{t, b\}, \end{cases} \quad (2)$$

where  $\langle \mathbf{F}_{c_h}, \mathbf{F}_i \rangle_h$  represents the same 3D correlation volume construction operation as RAFT-Stereo, where the inner product of the features from  $\mathbf{F}_{c_h}$  and  $\mathbf{F}_i$  is taken by horizontally shifting the feature map  $\mathbf{F}_i$ . Similarly,  $\langle \mathbf{F}_{c_v}, \mathbf{F}_i \rangle_v$  represents the 3D correlation volume construction operation by vertically shifting the feature map  $\mathbf{F}_i$ . Consequently, the dimension of the correlation volumes  $\{C_l, C_r\}$  result in  $H \times W \times W$ , while the dimension of the correlation volumes  $\{C_t, C_b\}$  result in  $H \times W \times H$ . Subsequently, the average pooling of the last dimension is applied three times for each correlation volume to construct a correlation pyramid with four scales, which is described as  $C_i = \{C_i^1, C_i^2, C_i^3, C_i^4\}$ .

The derived four correlation pyramids  $\{C_l, C_r, C_t, C_b\}$  are fed into our proposed MDLF module, as shown in the upper-right part of Fig 3, to produce a fused local correlation feature from all computed correlations in different directions and scales, as detailed in the next subsection. Finally, akin to RAFT-Stereo, we initialize the disparity to zero and iteratively update the disparity through the GRU module, where the fused local correlation feature, the current disparity, and the context feature extracted from the center image by a context encoder are concatenated and fed into the GRU module.

We supervise our OPDNet in the same manner as RAFT-Stereo using the  $L_1$  loss between the ground-truth and the predicted disparity maps in each GRU iteration as

$$\mathcal{L} = \sum_{j=1}^N \gamma^{N-j} \|\mathbf{D}_{gt} - \mathbf{D}_j\|_1, \quad (3)$$

where  $N$  represents the number of GRU iterations,  $\mathbf{D}_{gt}$  and  $\mathbf{D}_j$  denote the ground-truth disparity map and the predicted disparity map in iteration  $j$ , respectively, and  $\gamma^{N-j}$  denotes the weight for each iteration, which increases with the number of iterations.

## 4.2 Multi-Direction Lookup Fusion Module

The upper-right part of Fig. 3 shows our proposed MDLF module comprising two components: multi-direction lookup and feature fusion attention (FFA) group.

The inputs to the MDLF module are the set of four correlation pyramids  $\{C_l, C_r, C_t, C_b\}$ . For each pyramid, local correlations are looked up based on the current disparity. Specifically, for the correlation volume of each scale in the pyramid, the length of  $(2r + 1)$  correlation value vector is extracted around the pixel position associated with the current disparity. Thus, by combining the correlation value vectors of all four scales, the length of  $4 \cdot (2r + 1)$  vector is derived for each pixel. We further concatenate the looked-up  $4 \cdot (2r + 1)$ -length vectors from all four pyramids, resulting in a  $16 \cdot (2r + 1)$ -length vector for each pixel. By combining all the pixels, the local correlation feature map  $\mathbf{F}_{cor}$  with the dimension of  $H \times W \times 16 \cdot (2r + 1)$  is derived and fed into the next FFA group. In the case of the QP sensor, the amount of disparity is the same, but the direction is opposite for the center-left and the center-right disparities as well as the center-top and the center-bottom disparities. Thus, we reverse the sign of the current disparity when looking up the correlations in  $\{C_l, C_r\}$  according to our definition of the disparity.

Subsequently, the derived local correlation feature map  $\mathbf{F}_{cor}$  is fed into the next FFA group, where channel-wise and pixel-wise attentions are employed to fuse the local correlations adaptively. Following [24], we utilize an FFA group, comprising three FFA blocks and a final convolutional layer, as shown in Fig 3. Each FFA block with skip connection is composed as

$$\tilde{\mathbf{F}}_{cor} = (\mathbf{F}_{cor} + \text{Conv}(\mathbf{F}_{cor})) \odot \mathbf{A}_c \odot \mathbf{A}_p + \mathbf{F}_{cor}, \quad (4)$$

where  $\tilde{\mathbf{F}}_{cor}$  is the output feature of the FFA block,  $\mathbf{A}_c$  is the channel-wise attention, and  $\mathbf{A}_p$  is the pixel-wise attention. All of them have the same dimension as the input feature  $\mathbf{F}_{cor}$  and the operation  $\odot$  represents element-wise multiplication. Specifically,  $\mathbf{A}_c$  is formed by copying  $1 \times 1 \times 16 \cdot (2r + 1)$ -sized channel-wise attention to all the pixels. Similarly,  $\mathbf{A}_p$  is formed by copying  $H \times W \times 1$ -sized pixel-wise attention to all the channels. Those attentions are element-wise multiplied with the feature map to adaptively fuse the local correlations in  $\mathbf{F}_{cor}$  by learned attentions. To derive  $\mathbf{A}_c$  and  $\mathbf{A}_p$ , we adopt the same manner as [24]. The output from the final (i.e. the third) FFA block is then passed through a convolutional layer with skip connection as

$$\mathbf{F}'_{cor} = \text{Conv}(\tilde{\mathbf{F}}_{cor}) + \mathbf{F}_{cor}, \quad (5)$$

where  $\mathbf{F}'_{cor}$  is the final output of the MDLF module.

## 5 Experimental Results

### 5.1 Settings

**Camera and Training Data Settings.** An Olympus OM-1 camera with a ZUIKO DIGITAL 25mm F1.8 lens was employed to capture real-world QP data. The camera settings include the F-number of 1.8 and the focal length of 25mm with the focus distance set at 4m. Due to the huge size of the full-resolution images ( $5184 \times 3888$  pixels), the captured images were resized to one-third of their original size to facilitate the processing by the network. The pixel size was computed as the quotient of the sensor width and the horizontal resolution, where the sensor width is 0.0174m and the horizontal resolution after the post-resizing is 1728, resulting in the pixel size of  $1.01e^{-5}$ m.

For the generation of the synthetic QP dataset, we utilized all-in-focus images and depth maps provided in the Hypersim dataset [29]. During the generation process, the camera parameters identical to those of the real Olympus camera were applied. The depth range was set to 0.5-50m and only the scenes within this range were used. The minimal unit of the PSF radius was set to 0.01 pixels to precisely simulate the PSF kernels in high resolution. The generated synthetic QP dataset consists of 377 scenes of  $1024 \times 768$  pixels. The dataset was divided into 301 scenes for training, 38 scenes for validation, and the rest 38 scenes for testing, respectively. Additionally, a test set with noise was generated by adding Gaussian noise with a variance of 0.01 to evaluate the robustness against noise, which is inevitable in real data.

**Training Details.** For training our proposed QPDNet, we set the gamma value in Eq. 3 as 0.9. The input images were randomly cropped to dimensions of  $452 \times 452$ . Regarding training parameters, the learning rate was set to  $2e^{-4}$ , the weight decay was configured at  $1e^{-5}$ , and the batch size was set as 4. We iterated the GRU module eight times during both the training and the testing phases. The network was trained over a total of 265 epochs. The training took roughly 60 hours using a single NVIDIA GeForce RTX 4090 GPU.

**Compared Methods.** We compared our QPDNet with existing disparity estimation methods. Given the absence of methods specifically tailored for QP data, our comparison encompasses stereo methods and DP methods.

For the stereo methods, we selected RAFT-Stereo [13], which is the baseline architecture of our QPDNet, and IGEV-Stereo [61], which is another state-of-the-art method. To fairly compare the results with ours on the center-image-aligned disparity maps, we mixed the center-left and the center-right image pairs as the input data to train a single stereo network. Then, during the testing phase, the final center-image-aligned disparity map was derived by simply averaging the two disparity maps predicted from the center-left and the center-right image pairs.

For the DP methods, we compared MDD [23], which is an optimization-based method and estimates the blur kernel size map of the DP image, from which the disparity is derived with scale ambiguity. We also compared with SFBD [9], which is a state-of-the-art learning-based method trained in a self-supervised manner. Because the training code of SFBD is not publicly available, we utilized the pre-trained SFBD model for disparity estimation. Furthermore, we performed supervised training of the SFBD model only using DP (i.e. center-left and center-right) images among our training data. During this supervised training process, we replaced the photometric loss of the original SFBD with the supervised  $L_1$  loss, while maintaining the other kernel-split symmetry loss and smoothness loss as detailed in the original paper.

**Evaluation Metrics.** For the methods except for MDD that can directly estimate the disparity, we used the mean absolute error (MAE), the root mean squared error (RMSE), and  $d_{0.5}$ ,  $d_1$ , and  $d_2$  metrics, which describe the error percentage bigger than the thresholds of 0.5, 1.0, and 2.0 pixels, respectively. To compare with the MDD method which only can estimate the disparity with scale ambiguity, we adopted the affine invariant metrics of  $AI(1)$  and  $AI(2)$  in the MDD paper [23]. The  $AI(q)$  is defined as

$$AI(q) = \min_{a,b} \left( \frac{\sum_{(x,y)} |D_{gt}(x,y) - (a\hat{D}(x,y) + b)|^q}{N_I} \right)^{\frac{1}{q}}, \quad (6)$$

where  $N_I$  is the total number of image pixels,  $D_{gt}$  is the ground-truth disparity, and  $\hat{D}$  is the



Input	MDL	FFA	w/o noise					w/ noise				
			MAE	RMSE	d0.5	d1	d2	MAE	RMSE	d0.5	d1	d2
CL,CR			0.030	0.163	0.840	0.368	0.137	0.148	0.510	4.932	2.613	1.340
CLR	✓		0.028	0.151	0.764	0.343	0.128	0.094	0.334	2.782	1.260	0.579
CLR	✓	✓	0.027	0.144	0.762	0.341	0.117	0.102	0.291	3.866	1.493	0.450
CLRTB	✓		0.026	0.143	0.717	0.319	0.118	0.088	0.309	2.649	1.115	0.492
CLRTB	✓	✓	<b>0.025</b>	<b>0.142</b>	<b>0.703</b>	<b>0.317</b>	<b>0.116</b>	<b>0.074</b>	<b>0.264</b>	<b>2.129</b>	<b>0.956</b>	<b>0.366</b>

Table 1: The results of an ablation study.

estimated disparity. When  $q = 2$ ,  $a$  and  $b$  are obtained by a least squares method. When  $q = 1$ ,  $a$  and  $b$  are computed using iteratively re-weighted least squares.

## 5.2 Ablation Study

To validate the efficacy of each component of our QPDNet, we conducted an ablation study. Table 1 summarizes the performance of various configurations. The first row represents the baseline method, which is a simple adoption of RAFT-Stereo [13] to DP data, as explained in Sec. 5.1. The second row represents the method that adopts our multi-direction lookup (MDL) to the center-left and the center-right image pairs (i.e., the DP sensor configuration). The third row represents the method that further adopts the FFA group after the MDL. This method is the DP sensor version of our proposed architecture. Comparing these three methods, we can confirm that the disparity estimation accuracy is improved from the first row to the third row, validating the effectiveness of MDL and FFA even for the DP sensor configuration.

The fourth row represents the method using the QP data as the inputs. This method applies our MDL to all of the center-left, the center-right, the center-top, and the center-bottom image pairs. The last row represents our final proposal (i.e., QPDNet) that applies both MDL and FFA to the QP data. From the results, we can confirm that our QPDNet provides the best performance, especially showing the robustness to noise.

## 5.3 Comparison with Previous Methods

**Evaluation on Synthetic Data.** Table 2 and Fig. 4 show quantitative and visual results on the noise-free synthetic test dataset. In the noise-free testing results, the pre-trained SFBD\* shows worse  $AI(q)$  performance than the optimization-based method of MDD. In contrast, our trained SFBD\*\* exhibits improved performance compared to the pre-trained SFBD\*. RAFT-Stereo and IGEV-Stereo, which were also directly trained on our training set, show better performance than SFBD\*\*. Our proposed QPDNet outperforms the other methods on all evaluated metrics for the noise-free case.

As the disparities are quite small in the QP data, the differences among various methods are subtle under the noise-free condition. However, when subjected to testing data with noise as shown in Table 3, the robustness of each method becomes more evident. As illustrated in Table 3, the observed tendencies remain similar to those of the noise-free results, though SFBD\*\* outperforms RAFT-Stereo and IGEV-Stereo for the noisy case. Notably, our QPDNet maintains its superiority, demonstrating enhanced performance and robustness. Furthermore, visual comparisons depicted in Fig. 5 highlight the superior performance of our QPDNet to the other methods.



Methods	MAE	RMSE	$d_{0.5}$	$d_1$	$d_2$	AI(1)	AI(2)
RAFT-Stereo [13]	0.030	0.163	0.840	0.368	0.137	0.030	0.082
IGEV-Stereo [81]	0.035	0.179	0.854	0.376	0.165	0.035	0.093
MDD [23]	—	—	—	—	—	0.208	0.324
SFBD* [9]	0.290	0.754	7.315	3.470	0.876	0.262	0.430
SFBD** [9]	0.038	0.187	1.085	0.472	0.177	0.041	0.107
QPDNet (Ours)	<b>0.025</b>	<b>0.142</b>	<b>0.703</b>	<b>0.317</b>	<b>0.116</b>	<b>0.025</b>	<b>0.074</b>

Table 2: The quantitative comparisons on the noise-free synthetic dataset. SFBD\* indicates the utilization of pre-trained weights, while SFBD\*\* refers to the model that was trained on our training data in a supervised manner.

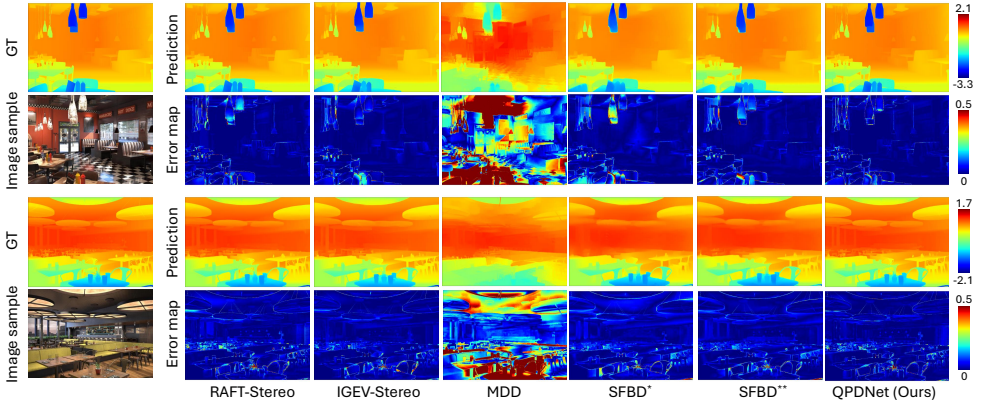


Figure 4: Visual comparisons on the noise-free synthetic dataset.

Methods	MAE	RMSE	$d_{0.5}$	$d_1$	$d_2$	AI(1)	AI(2)
RAFT-Stereo [13]	0.148	0.510	4.932	2.613	1.340	0.144	0.271
IGEV-Stereo [81]	0.141	0.452	4.648	2.056	<b>0.355</b>	0.136	0.256
MDD [23]	—	—	—	—	—	0.254	0.367
SFBD* [9]	0.419	0.837	23.266	8.764	3.933	0.357	0.528
SFBD** [9]	0.110	0.276	3.011	1.046	0.309	0.103	0.191
QPDNet (Ours)	<b>0.074</b>	<b>0.264</b>	<b>2.129</b>	<b>0.956</b>	0.366	<b>0.072</b>	<b>0.153</b>

Table 3: The quantitative comparisons on the synthetic dataset with Gaussian noise. SFBD\* indicates the utilization of pre-trained weights, while SFBD\*\* refers to the model that was trained on our training data in a supervised manner.

**Evaluation on Real Scene Data.** To further evaluate the robustness of our QPDNet, we conducted evaluations using real-world data. Because obtaining ground-truth disparity maps aligned with the real QP sensor is difficult, our evaluation relies on qualitative visual comparisons. Figure 6 illustrates the visual outcomes derived from the real-world data. Overall, the optimization-based MDD method struggles to produce accurate disparity maps. In the second row of the figure, all the methods except MDD produce satisfactory estimation results. However, in the first and third rows, it is evident that our QPDNet consistently predicts better and sharper disparity maps in real-world scenarios.

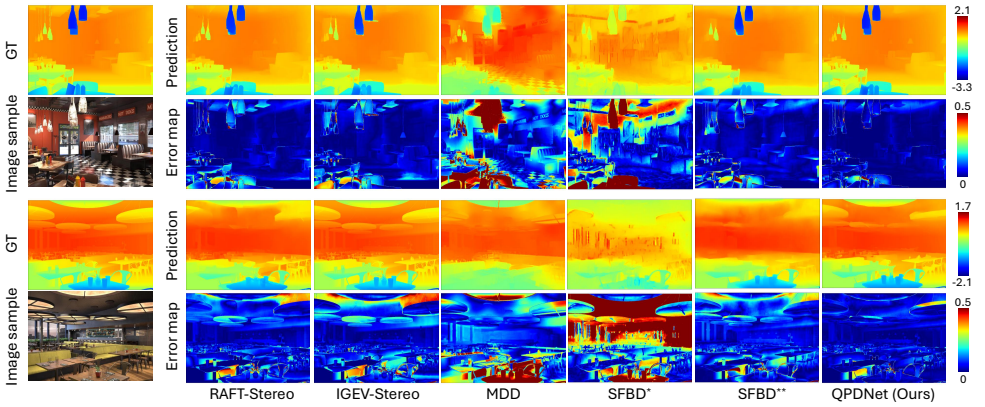


Figure 5: Visual comparisons on the synthetic data with Gaussian noise.

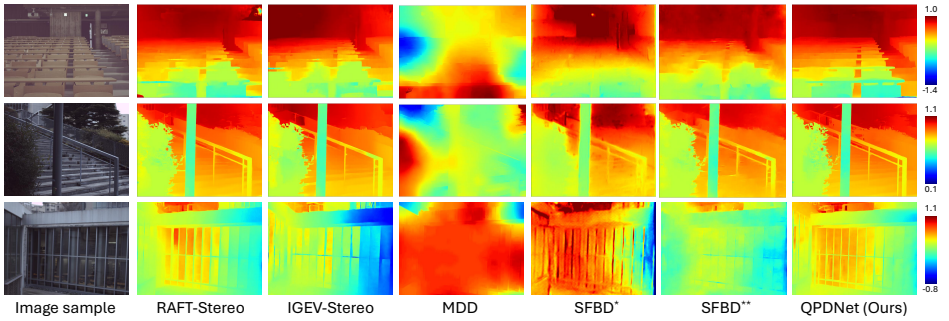


Figure 6: Visual comparisons on real-scene data.

## 6 Conclusion

In this paper, we have proposed a novel network, QPDNet, to estimate the disparity using a QP sensor. Our proposed QPDNet leverages the multi-directional disparity information provided by the QP data. Specifically, we have constructed multi-directional stereo-matching correlation volumes and effectively fused them with a novel MDFL module. To train and test QPDNet, we have constructed a synthetic QP dataset. Through extensive experiments, we have validated the effectiveness of our QPDNet. One of the possible future works includes the extension of QPDNet to a self-supervised method to better generalize to real-scene data, by using the data obtained by a real QP camera including non-ideal properties, such as noise, distorted PSFs, and unbalanced brightness.

## References

- [1] Abdullah Abuolaim and Michael S Brown. Defocus deblurring using dual-pixel data. In *European Conference on Computer Vision (ECCV)*, pages 111–126, 2020.
- [2] Abdullah Abuolaim, Mauricio Delbracio, Damien Kelly, Michael S Brown, and Peyman Milanfar. Learning to reduce defocus blur by realistically modeling dual-pixel

- data. In *IEEE/CVF International Conference on Computer Vision (ICCV)*, pages 2289–2298, 2021.
- [3] Jia-Ren Chang and Yong-Sheng Chen. Pyramid stereo matching network. In *IEEE/CVF Conference on Computer Vision and Pattern Recognition (CVPR)*, pages 5410–5418, 2018.
- [4] Chun-Fu Richard Chen, Quanfu Fan, and Rameswar Panda. CrossViT: Cross-attention multi-scale vision transformer for image classification. In *IEEE/CVF International Conference on Computer Vision (ICCV)*, pages 357–366, 2021.
- [5] Rahul Garg, Neal Wadhwa, Sameer Ansari, and Jonathan T Barron. Learning single camera depth estimation using dual-pixels. In *IEEE/CVF International Conference on Computer Vision (ICCV)*, pages 7628–7637, 2019.
- [6] Xiaoyang Guo, Kai Yang, Wukui Yang, Xiaogang Wang, and Hongsheng Li. Group-wise correlation stereo network. In *IEEE/CVF Conference on Computer Vision and Pattern Recognition (CVPR)*, pages 3273–3282, 2019.
- [7] Jason Holloway, Kaushik Mitra, Sanjeev J. Koppal, and Ashok Narayanan Veeraraghavan. Generalized Assorted Camera Arrays: Robust cross-channel registration and applications. *IEEE Transactions on Image Processing*, 24(3):823–835, 2014.
- [8] Minjun Kang, Jaesung Choe, Hyowon Ha, Hae-Gon Jeon, Sunghoon Im, In So Kweon, and Kuk-Jin Yoon. Facial depth and normal estimation using single dual-pixel camera. In *European Conference on Computer Vision (ECCV)*, pages 181–200, 2022.
- [9] Donggun Kim, Hyeonjoong Jang, Inchul Kim, and Min H. Kim. Spatio-focal bidirectional disparity estimation from a dual-pixel image. In *IEEE/CVF Conference on Computer Vision and Pattern Recognition (CVPR)*, pages 5023–5032, 2023.
- [10] Junyong Lee, Sungkil Lee, Sunghyun Cho, and Seungyong Lee. Deep defocus map estimation using domain adaptation. In *IEEE/CVF Conference on Computer Vision and Pattern Recognition (CVPR)*, pages 12222–12230, 2019.
- [11] Yizhou Li, Yusuke Monno, and Masatoshi Okutomi. Dual-pixel raindrop removal. In *British Machine Vision Conference Proceedings (BMVC)*, pages 439:1–13, 2022.
- [12] Zhaoshuo Li, Xingtong Liu, Nathan Drenkow, Andy Ding, Francis X Creighton, Russell H Taylor, and Mathias Unberath. Revisiting stereo depth estimation from a sequence-to-sequence perspective with transformers. In *IEEE/CVF International Conference on Computer Vision (ICCV)*, pages 6197–6206, 2021.
- [13] Lahav Lipson, Zachary Teed, and Jia Deng. RAFT-Stereo: Multilevel recurrent field transforms for stereo matching. In *International Conference on 3D Vision (3DV)*, pages 218–227, 2021.
- [14] Zihua Liu, Songyan Zhang, Zhicheng Wang, and Masatoshi Okutomi. Digging into normal incorporated stereo matching. In *ACM International Conference on Multimedia (ACMMM)*, pages 6050–6060, 2022.

- [15] Zihua Liu, Yizhou Li, and Masatoshi Okutomi. Global occlusion-aware transformer for robust stereo matching. In *IEEE/CVF Winter Conference on Applications of Computer Vision (WACV)*, pages 3535–3544, 2024.
- [16] Yawen Lu, Garrett Milliron, John Slagter, and Guoyu Lu. Self-supervised single-image depth estimation from focus and defocus clues. *IEEE Robotics and Automation Letters*, 6(4):6281–6288, 2021.
- [17] Nikolaus Mayer, Eddy Ilg, Philip Hausser, Philipp Fischer, Daniel Cremers, Alexey Dosovitskiy, and Thomas Brox. A large dataset to train convolutional networks for disparity, optical flow, and scene flow estimation. In *IEEE/CVF Conference on Computer Vision and Pattern Recognition (CVPR)*, pages 4040–4048, 2016.
- [18] Nikolaus Mayer, Eddy Ilg, Philip Hausser, Philipp Fischer, Daniel Cremers, Alexey Dosovitskiy, and Thomas Brox. End-to-end learning of geometry and context for deep stereo regression. In *IEEE/CVF International Conference on Computer Vision (ICCV)*, pages 66–75, 2017.
- [19] Tetuya Okawa, Susumu Ooki, Hiroaki Yamajo, Masakazu Kawada, Masayuki Tachi, Kazuhiro Goi, Takatsugu Yamasaki, Hiroki Iwashita, Masahiko Nakamizo, Takayuki Ogasahara, et al. A 1/2inch 48m all pda f cmos image sensor using 0.8 $\mu$ m quad bayer coding 2 $\times$ 2ocel with 1.0lux minimum af illuminance level. In *IEEE International Electron Devices Meeting (IEDM)*, pages 16–3, 2019.
- [20] Masatoshi Okutomi and Takeo Kanade. A multiple-baseline stereo. *IEEE Transactions on Pattern Analysis and Machine Intelligence*, 15(4):353–363, 1993.
- [21] Liyuan Pan, Shah Chowdhury, Richard Hartley, Miaomiao Liu, Hongguang Zhang, and Hongdong Li. Dual Pixel Exploration: Simultaneous depth estimation and image restoration. In *IEEE/CVF Conference on Computer Vision and Pattern Recognition (CVPR)*, pages 4340–4349, 2021.
- [22] Abhijith Punnappurath and Michael S Brown. Reflection removal using a dual-pixel sensor. In *IEEE/CVF Conference on Computer Vision and Pattern Recognition (CVPR)*, pages 1556–1565, 2019.
- [23] Abhijith Punnappurath, Abdullah Abuolaim, Mahmoud Afifi, and Michael S. Brown. Modeling defocus-disparity in dual-pixel sensors. In *IEEE International Conference on Computational Photography (ICCP)*, pages 1–12, 2020.
- [24] Xu Qin, Zhilin Wang, Yuanchao Bai, Xiaodong Xie, and Huizhu Jia. FFA-Net: Feature fusion attention network for single image dehazing. In *AAAI Conference on Artificial Intelligence*, pages 11908–11915, 2020.
- [25] Mike Roberts, Jason Ramapuram, Anurag Ranjan, Atulit Kumar, Miguel Angel Bautista, Nathan Paczan, Russ Webb, and Joshua M. Susskind. Hypersim: A photorealistic synthetic dataset for holistic indoor scene understanding. In *IEEE/CVF International Conference on Computer Vision (ICCV)*, pages 10912–10922, 2021.
- [26] Zhelun Shen, Yuchao Dai, and Zhibo Rao. CFNet: Cascade and fused cost volume for robust stereo matching. In *IEEE/CVF Conference on Computer Vision and Pattern Recognition (CVPR)*, pages 13906–13915, 2021.

- [27] Nathan Silberman, Derek Hoiem, Pushmeet Kohli, and Rob Fergus. Indoor segmentation and support inference from rgb-d images. In *European Conference on Computer Vision (ECCV)*, pages 746–760, 2012.
- [28] Neal Wadhwa, Rahul Garg, David E Jacobs, Bryan E Feldman, Nori Kanazawa, Robert Carroll, Yair Movshovitz-Attias, Jonathan T Barron, Yael Pritch, and Marc Levoy. Synthetic depth-of-field with a single-camera mobile phone. *ACM Transactions on Graphics*, 37(4):1–13, 2018.
- [29] Shumian Xin, Neal Wadhwa, Tianfan Xue, Jonathan T Barron, Pratul P Srinivasan, Jiawen Chen, Ioannis Gkioulekas, and Rahul Garg. Defocus map estimation and deblurring from a single dual-pixel image. In *IEEE/CVF International Conference on Computer Vision (ICCV)*, pages 2228–2238, 2021.
- [30] Gangwei Xu, Junda Cheng, Peng Guo, and Xin Yang. Attention concatenation volume for accurate and efficient stereo matching. In *IEEE/CVF Conference on Computer Vision and Pattern Recognition (CVPR)*, pages 12981–12990, 2022.
- [31] Gangwei Xu, Xianqi Wang, Xiaohuan Ding, and Xin Yang. Iterative geometry encoding volume for stereo matching. In *IEEE/CVF Conference on Computer Vision and Pattern Recognition (CVPR)*, pages 21919–21928, 2023.
- [32] Haofei Xu, Jing Zhang, Jianfei Cai, Hamid Rezaatoughi, Fisher Yu, Dacheng Tao, and Andreas Geiger. Unifying flow, stereo and depth estimation. *IEEE Transactions on Pattern Analysis and Machine Intelligence*, 45(11):13941–13958, 2023.
- [33] Feihu Zhang, Victor Prisacariu, Ruigang Yang, and Philip HS Torr. GA-Net: Guided aggregation net for end-to-end stereo matching. In *IEEE/CVF Conference on Computer Vision and Pattern Recognition (CVPR)*, pages 185–194, 2019.
- [34] Yinda Zhang, Neal Wadhwa, Sergio Orts-Escolano, Christian Häne, Sean Fanello, and Rahul Garg. Du<sup>2</sup>Net: Learning depth estimation from dual-cameras and dual-pixels. In *European Conference on Computer Vision (ECCV)*, pages 582–598, 2020.
- [35] Jia Zheng, Junfei Zhang, Jing Li, Rui Tang, Shenghua Gao, and Zihan Zhou. Structured3D: A large photo-realistic dataset for structured 3d modeling. In *European Conference on Computer Vision (ECCV)*, pages 519–535, 2020.